Supplementary Information for

Directly wireless communication of human minds via non-invasive brain-computer-metasurface platform

Qian Ma *et* al.

This file includes:

Supplementary Note S1. Design of programmable element and architecture of EBCM

To achieve programmable controls of scattered fields, we employ a programmable 2-bit phase-control element, as depicted in Figs. S1a and S1b. Two PIN diodes (MACOM MADP-000907-14020) are embedded on the top metal layer to generate four distinct reflected phase responses, which can be regarded as the 2-bit digital states "0", "1", "2", and "3". Two sector-shaped branches are used in the bias lines, as shown in Fig. S1b, to block the RF signals. The marked dimensions in Figs. S1a and S1b are designed as: a=9.4 mm, b=7.7 mm, c=2.55 mm, P=12 mm, h1=1.5 mm, h2=0.7 mm, d=4 mm, e=2.1 mm, and r=3.5 mm. The top and bottom substrates are F4B (ε_r = 2.65, tanδ = 0.003) and FR4 (ε_r = 4.3, tanδ = 0.025), respectively. The simulated performance is shown in Figs. S1b and S1c, which is performed in commercial software, CST Microwave Studio. The periodic boundary conditions and plane-wave excitation are applied in the unit cell simulation. We use the RLC series model to mimic the switching state of the diode, and the specific values are: (1) ON state: R=2.2 Ω, L=0.32 nH, C=0; (2) OFF state: R=0, L=0.4 nH, C=0.04 pF. The amplitude responses in Fig. S1b are above -3dB among the operating frequency band, promising good reflecting efficiency. By modulating the on-off states of the PIN diodes, the related reflection phase responses at 9.2 GHz are -140.3°, -69.4°, 31.9°, and 112.3°, respectively, as shown in Fig. S1c, with about 90° difference between adjacent states.
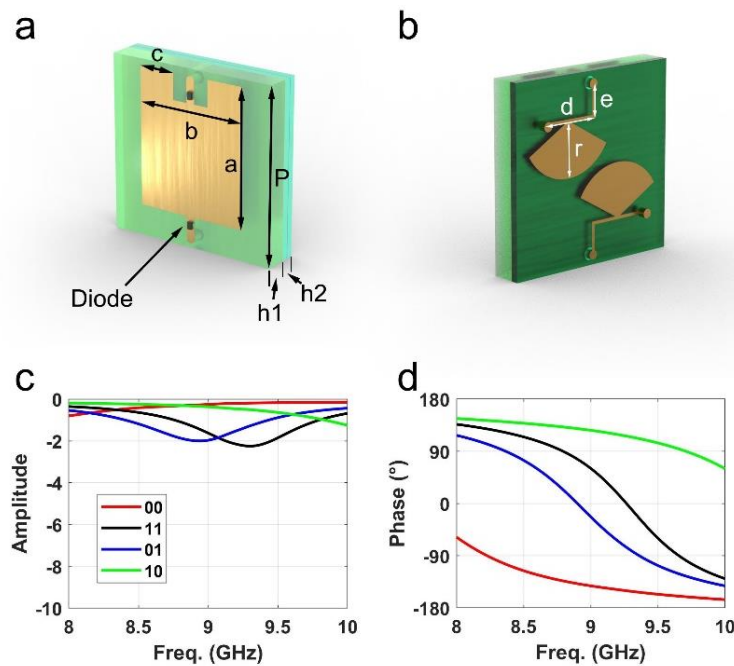

Fig. S1. The 2-bit programmable element and its EM responses. (a) and (b) The programmable element for

2-bit phase manipulations, where two PIN diodes are integrated. (c) and (d) The reflection amplitude and phase responses with four on-off states of diodes.

To clearly exhibit the architecture of EBCM, we provide a detailed control illustration from the visual stimuli used to evoke P300 potentials to the programmable EM functions. As shown in Fig. S2, the operator is presented with a series of frames sequentially, in which each frame contains several highlight-green buttons. If the operator stares at a button, its unique time sequence code can be recognized based on P300 brain signal analysis. A P300 potential usually occurs at around 300 ms after a low-probability target stimulus which is mixed with high-probability non-target stimuli, including not only visual, but also an auditory or somatosensory stimulus. An electroencephalographic (EEG) cap with 30-channel electrodes is equipped on the scalp of the operator, whose EEG signals are referenced to the right mastoid, to detect EEG signal. The collected signals are real-time preprocessed and then decoded using Bayesian linear regression algorithm by a computer. After the processing, the computer recognizes the button that the operator gazed and send the corresponding instructions to the FPGA, which manages the detailed pattern configuration of the metasurface. Four typical schemes including coding, beam-scanning, multi-function and communication are designed, where each scheme has a distinct set of instruction function. One of the detailed visual coding screens (the beam-scanning scheme) is given for example in the right of Fig. S2, composed of 4*10 buttons. The measured EEG signals from six typical channels are presented in Fig. S2, corresponding to the beam-scanning scheme.
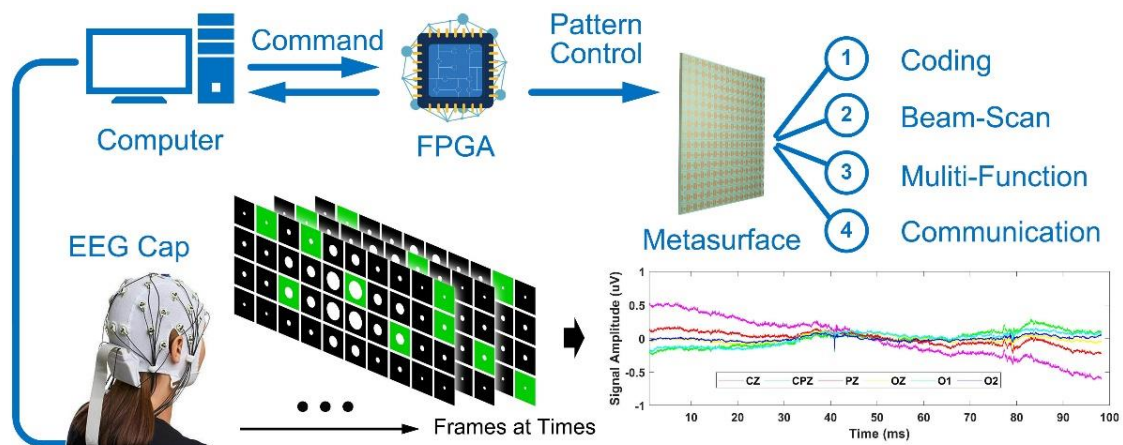

Fig. S2. The control mechanism of EBCM from brain signal stimulus to diverse EM functions. The sequential stimulus frames in time domain generate the specific brain signals.

Supplementary Note S2. Text-interface and the receiving GUI for wireless communication

The text-interface is composed of 4×10 buttons as shown in Fig. S3, which contains 26 letters, numbers 0-9 and several symbols. The buttons are sequentially encoded as "A001A" to "A040A" in the serial-port communication between BCI device and metasurface. Once the FPGA of metasurface detects the code, like "A001A" for example, the metasurface translates the code into American Standard Code for Information Interchange (ASCII) as "0100 0001", related to the letter "A". Similarly, the numbers and symbols are also encoded within ASCII in the text communication.
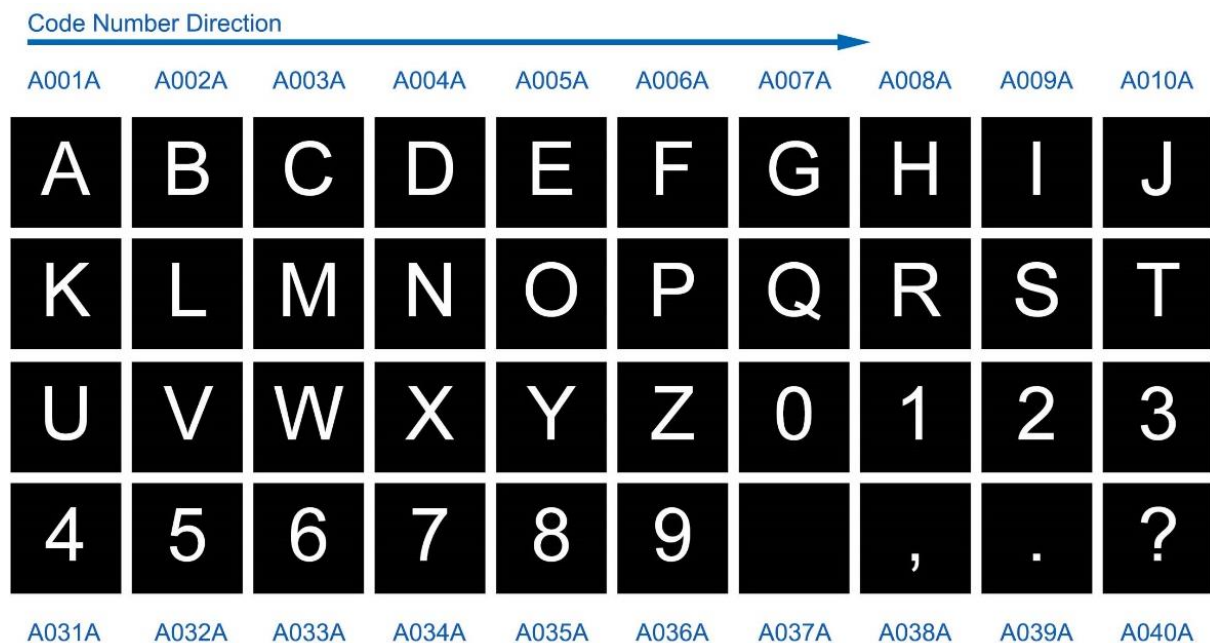

Fig. S3. The text interface in the communication scheme. The 40 buttons are first encoded as "A001A" to "A040A", and translated into ASCII codes in wireless communication.

To exhibit the received results, we design a receiving GUI as shown in Fig. S4, where the left window displays the last transmitted letter, and the right window shows the whole transmitted text.
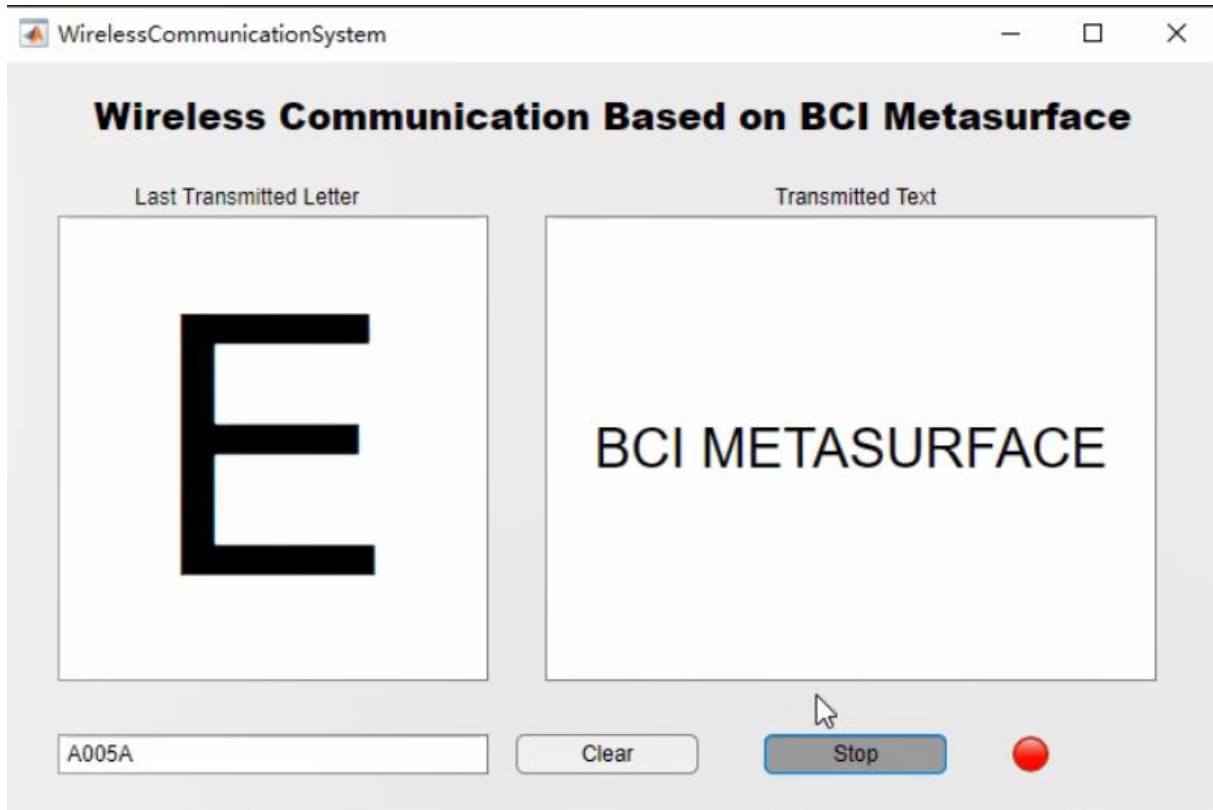
Fig. S4. The receiving GUI in wireless communication scheme.

Supplementary Note S3. The metasurface embedded with light emitting diodes (LEDs) for control demonstrations

The core of the EBCM is to transform the information from the brain signals to the EM functions, which is highly related to the coding patterns of metasurface. However, for the conventional PIN diodes used in microwave manipulation, it is hard to distinguish the coding pattern arranged on the metasurface directly. Therefore, in the BCI-jointed demonstration, we employ a metasurface with the same configuration but integrated with light emitting diodes (LEDs) instead of PIN diodes to directly display the coding pattern after the BCI control, which offers a clear visual demonstration method of the relative EM functions manipulation. In the metasurface configuration, the diodes in each element are all independently controlled by two FPGAs with 800 input/output (I/O) ports (each FPGA offers 400 ports). The FPGAs is fixed on the back side of the metasurface, as showed in Fig. S5. Since each port of FPGA is able to provide at least 3.3 V driving voltage and 5mA current, both PIN diodes (MACOM 000907-14020) and LEDs can be driven by the same FPGA configuration.

Fig. S5. The photograph of the fabricated metasurface sample loaded with LEDs. (a) The back view of the LED version metasurface. (b) The front view of the LED version metasurface.

For experimental EM measurement and verifications, a metasurface with PIN diodes (MACOM 000907-14020) is fabricated as shown in Fig. S6 with both the front and back view. The metasurface of LED version and PIN-diode version are both fabricated within (PCB) technology but embedded with different components. On the back of the metasurface, two FPGA sockets are integrated for FPGA modules as depicted in Fig. S6b.
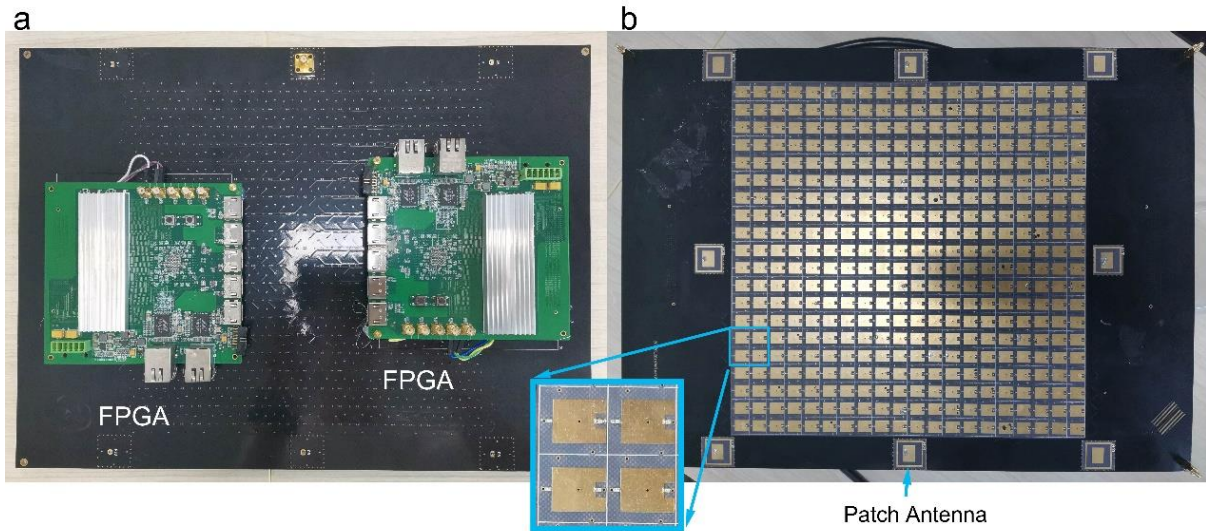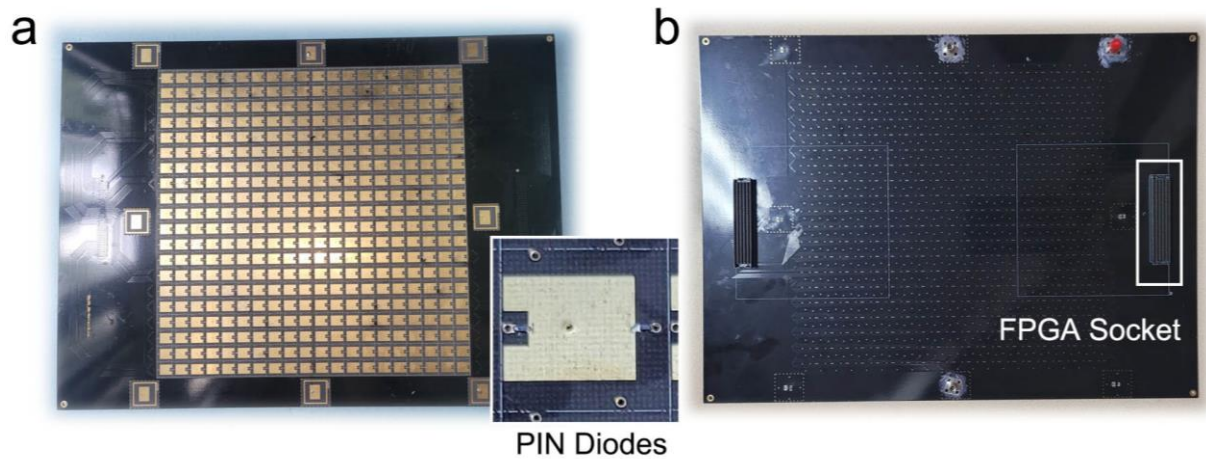

Fig. S6. The photograph of the fabricated metasurface sample loaded with PIN diodes. (a) The front view of the PIN-diode version metasurface. (b) The back view of the PIN-diode version metasurface.

Supplementary Note S4. The visual interface for the beam-scanning scheme and measured multiple function scheme

In the visual beam-scanning scheme, the metasurface switches the coding patterns for the desired beam-scattering angle according to the instruction from BCI devices. We design a symmetric beam-control interface in Fig. S7. We assume a space wireless communication or radar scanning scenario that requiring the real-time beam-scanning. Hence, we use a background picture of sky and circular spot buttons to indicate the scanning directions. As depicted in Fig. S7, the interface composed of 4×10 buttons are divided into 4 quadrants, each of which provides two levels (15° and 30°) along vertical-axis (ϕ-axis) and five levels (5°, 10°, 20°, 30° and 40°) along horizontal-axis (θ-axis). To avoid the extra interference, the buttons are design as circular spot with different sizes to indicate the distinct scattering directions. We have recorded a video of such visually-controlled beam deflections toward multiple directions (see Supplementary Movie S2). More simulation results are given in Supplementary Note S5 and EEG data in the experiments are listed in Supplementary Note S8 and measured data are given in Supplementary Note S7.
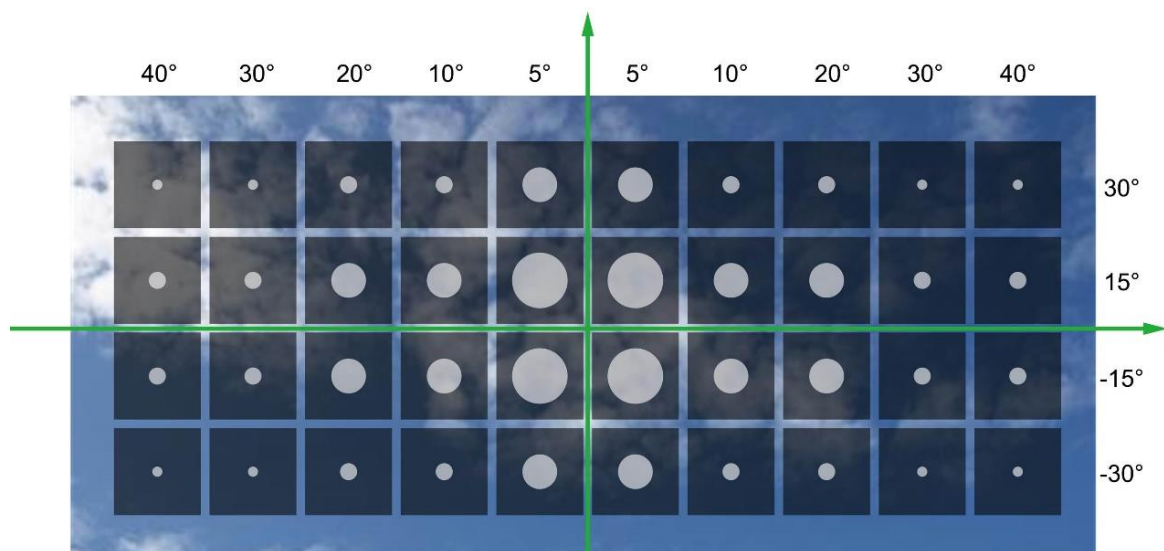

Fig. S7. The visual interface for visual beam-scanning scheme.

We present a GUI in Fig. 3a, demonstrating three different and switchable wavefronts: single beam, orbital-angular-momentum (OAM) beam, and radar-cross-section (RCS) modulation. The GUI in Fig. S8 for brain signal detection is designed with the central two rows. In the

control GUI, we provide 12 single-beam directions labeled as 'X±1, X±2, X±3' and 'Y±1, Y±2, Y±3', where 'X' and 'Y' respectively represent the beam deflections along the x-axis and y-axis, '+' and '−' mean the deflections along the positive and negative axes, and digits '1-3' denote three levels of deflecting angles at 15°, 30° and 45°. We provide four levels of RCS reduction labeled as '01-04', corresponding to four reflected amplitudes of the scattering intensity. In addition to the functions mentioned above, four modes of OAM beams are designed as 'OAM-1, OAM+1, OAM-2, OAM+2', which refer to the topological charges of -1, +1, -2 and +2, respectively. The coding patterns of these three typical wavefronts are listed in Supplementary Note S6.
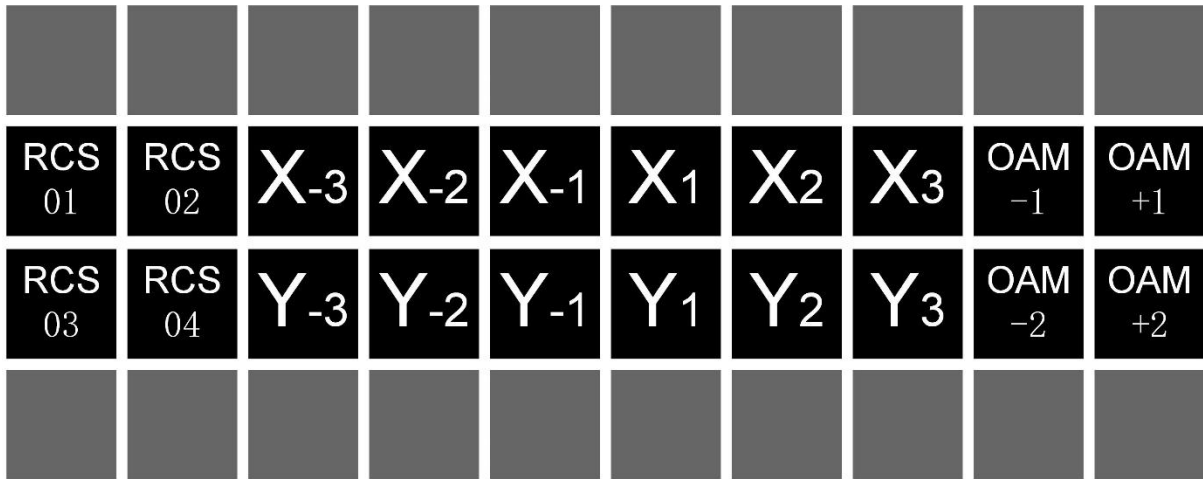
Fig. S8. The visual interface for multiple EM function scheme.

Supplementary Note S5. The simulated results of the beam-scanning scheme

To show the performance of the scattering field control using presented metasurface, we exhibit the numerical simulation results of the deflection angles in the second quadrant, as illustrated in Fig. S9a-S9j, expressed in 2D far-field data. The related coding patterns of these 10 deflecting directions are given in Fig. S9. The target scattering directions of these 10 patterns are (-5°, 15°), (-10°, 15°), (-20°, 15°), (-30°, 15°), (-40°, 15°), (-5°, 30°), (-10°, 30°), (-20°, 30°), (-30°, 30°), (-40°, 30°). According to the calculated results, the 10 beam-deflecting cases are (-4.8°, 14.2°), (-9.6°, 14.4°), (-20.1°, 16.8°), (-29.8°, 16.7°), (-40.7°, 16.5°), (-4.7°, 31°), (-9.8°, 30.8°), (-20.6°, 31.2°), (-31.6°, 30.7°), (-40.2°, 30.4°), proved to be consistent with the design goals. The metasurface patterns are pre-designed using the smart metasurface algorithm.
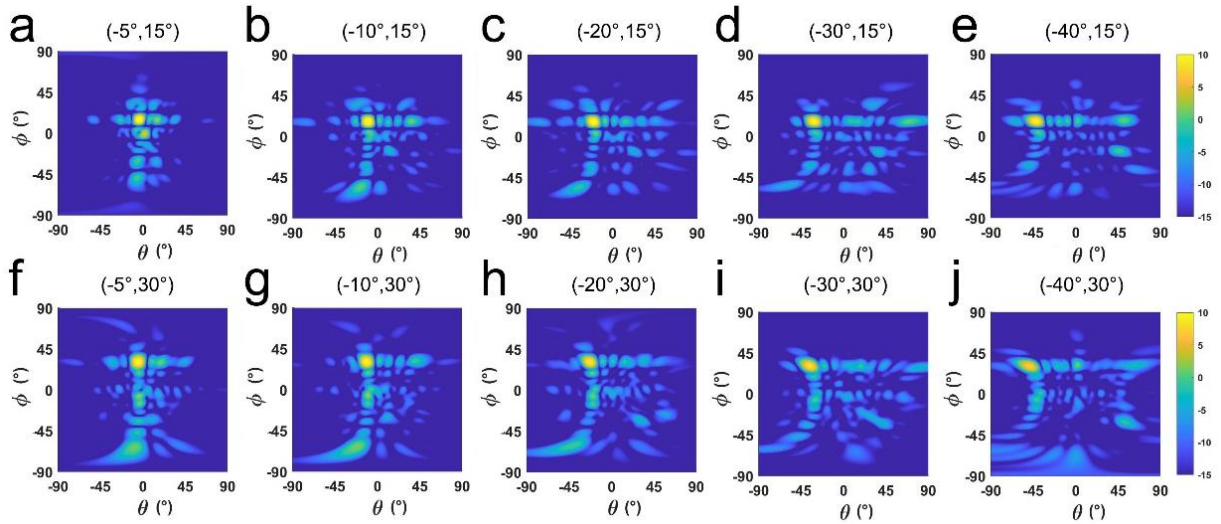
Fig. S9. The simulated scattering fields of the 10 distinct directions in the second quadrant. (a)-(j) The designed direction angles of the single-beam respectively are (-5°, 15°), (-10°, 15°), (-20°, 15°), (-30°, 15°), (-40°, 15°), (-5°, 30°), (-10°, 30°), (-20°, 30°), (-30°, 30°), (-40°, 30°).

Supplementary Note S6. Coding patterns and the related scattering results in the beam-scanning scheme and the multi-function scheme

The coding patterns for the different beam-scattering angles are calculated based on the self-adaptively pattern design algorithm [S3]. Considering the symmetry of the beam-scattering in four quadrants, we give the 10 coding patterns in the second quadrant. The coding patterns listed in Fig. S10a-S10l respectively are the beam pointed at (-5°, 15°), (-5°, 30°), (-10°, 15°), (-10°, 30°), (-20°, 15°), (-20°, 30°), (-30°, 15°), (-30°, 30°), (-40°, 15°), (-40°, 30°).
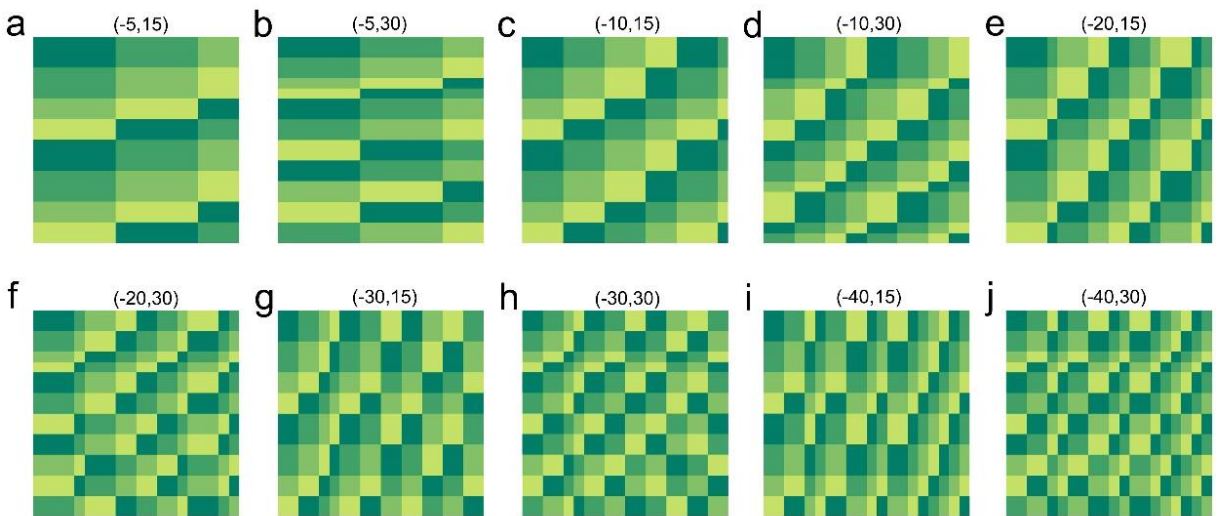
Fig. S10. The designed coding patterns for the scattering directions in the second quadrant. Four different colors indicate the four gradient phase responses of 0°, 90°, 180°, 270°. (a)-(j) The scattering directions

respectively point at (-5°, 15°), (-5°, 30°), (-10°, 15°), (-10°, 30°), (-20°, 15°), (-20°, 30°), (-30°, 15°), (-30°, 30°), (-40°, 15°), (-40°, 30°).

The coding patterns in the multi-function scheme are designed as shown in Fig. S11. Here we exhibit four levels of RCS reduction patterns as listed in Figs. S11a-S11d, named as RCS 01-04. Four OAM modes including ±1 and ±2 orders as given in Figs. S10e-S10h, where the direction and period of the phase vortex can be clearly observed. Considering the symmetry of the single-beam pattern, we provide three patterns deflecting along x-axis as 15°, 30°, 45° respectively, as given in Figs. S11i-S11l. For the modes in which the beam points to the negative semi-axis of the x-axis, the encoding patterns have a 180° rotation relationship with Figs. S11i-S11l. Similarly, for the beam scattering at y-axis, the coding patterns a 90° rotation relationship with Figs. S11i-S11l.
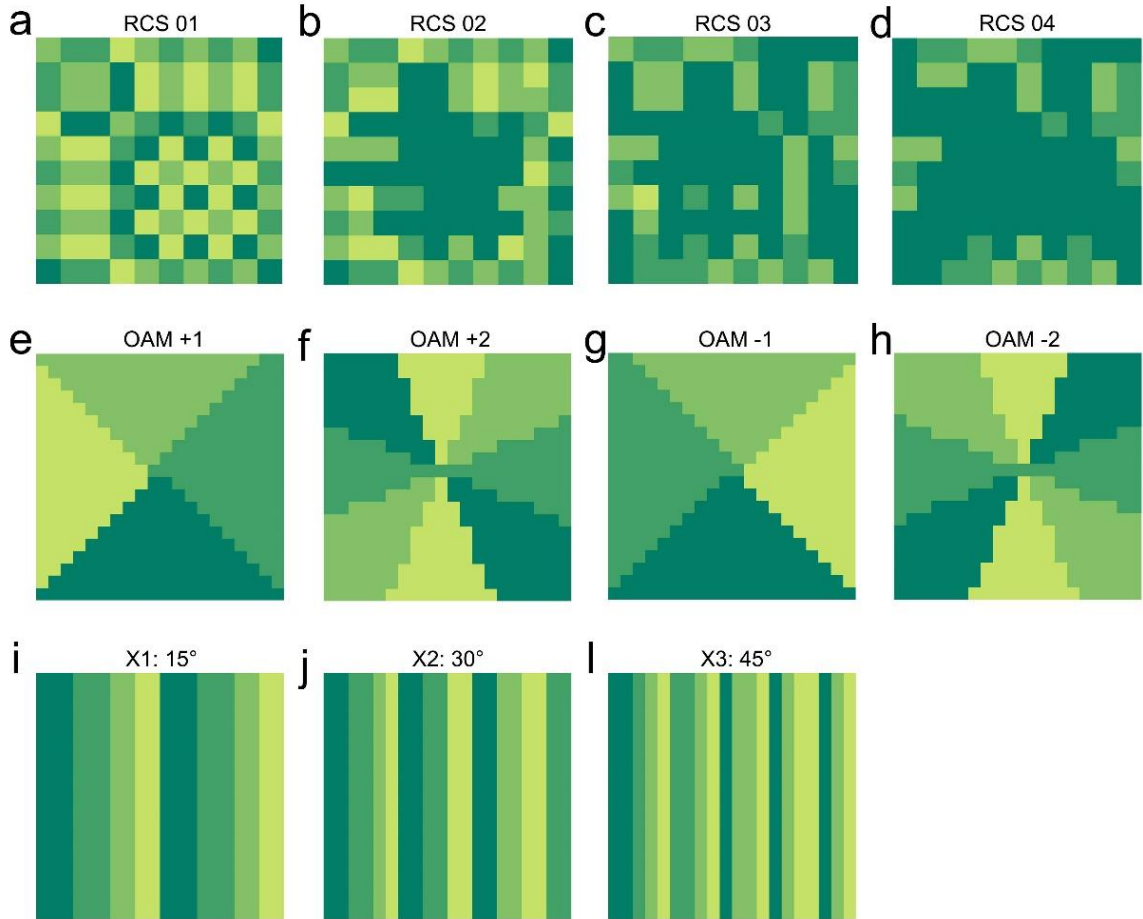

Fig. S11. The coding patterns in the multi-function scheme. Four different colors indicate the four gradient phase responses of 0°, 90°, 180°, 270°. (a)-(d) The four levels of the RCS reduction patterns with different reflection intensity. (e)-(f) The four coding patterns of different OAM modes. (i)-(l) The three coding patterns single-beam deflection aiming at 15°, 30°, 45° respectively.

Supplementary Note S7. Far-field and near-field measurement results

To experimentally demonstrate the EM scattering performance presented in this work, we perform the far-field measurements for the beam deflection, RCS reduction and OAM beams. In the visual beam-scanning scheme, four typical directions are measured, as shown in Figs. S12a-S1ad, related to the angles of (-5°, 15°), (-5°, 30°), (-10°, 15°), (-10°, 30°). In Figs. S12a and S12b, the metasurface is first rotated 5 to measure the beam deflection on ϕ-axis. Similarly, in Figs. S12c and S12d, the metasurface is first rotated 10 to perform the measurements. In the versatile wavefront syntheses, as given in Figs. S12e-S12g, the far-field results of beam deflection at 15°, 30°, and 45° show good agreement with the simulation data marked in blue. The four levels of RCS reduction (RCS 01-04) also present high consistency on the reflected intensity, as shown in Figs. S12h- S12k. The measured intensities of the four cases are -14.9 dB, -12.2 dB, -9.3 dB, and -5.8 dB respectively. It should be noted that these measured values are compared to the reflected intensity of a metal plate with the same dimension. Besides, the near-field measurements are also carried out for the verifications of OAM performance, as listed in Figs. S12l- S12o. The central phase vortex can be clearly observed, validating the good OAM beam characteristics. For the +1 OAM mode, the vortex phase distribution has a 360° variety; for the +2 OAM mode, the vortex phase distribution has a 720° variety. Compared to the simulated results, measurement results show slight errors, mainly due to the following reasons: (1) The fabrication error from the printed circuit board (PCB) process and manual soldering, which may introduce inconsistency compared to simulation; (2) The measurement error including the inaccuracy of manual operation, instrument error and so on; (3) The non-ideal plane wave from the horn antenna which causes slight unevenness of phase distribution. We can also observe that the background noise seems a little large in three single-beam deflection patterns, which mainly results from the limited size of metasurface and the long distance between the metasurface and feed antenna. The final reflected energy is relatively low therefore the background noise is a little apparent. Nevertheless, the beam pointing angles and the energy distribution are in good agreement.
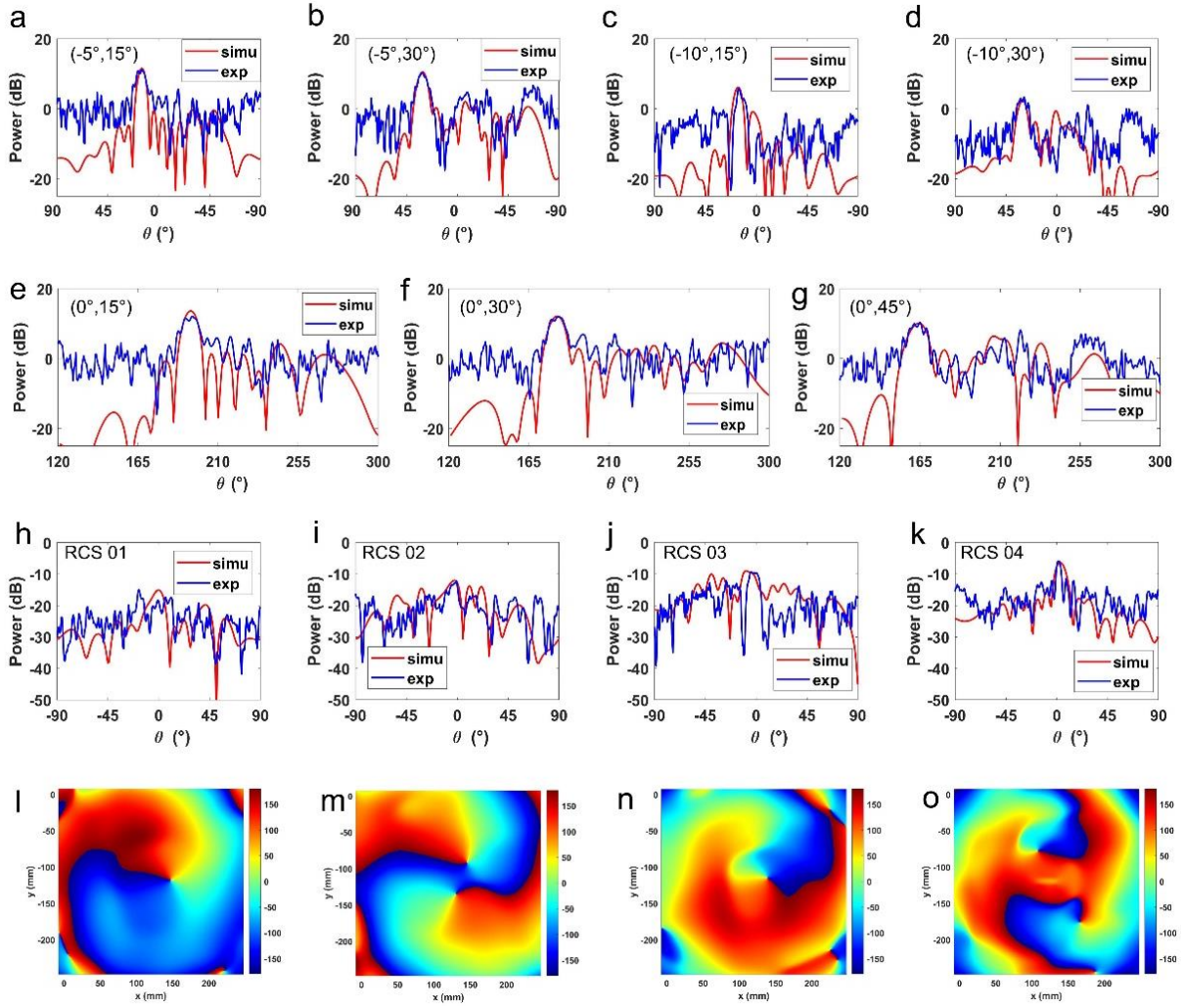
Fig. S12. The measured results. (a)-(d) The comparison of the simulation and measurement in the visual beam-scanning, related to the directions of (-5°, 15°), (-5°, 30°), (-10°, 15°), (-10°, 30°). (e)-(g) The comparison of the single-beam patterns of 15°, 30°, 45°. (h)-(k) The simulated and measured data of RCS patterns 01-04. (h)-(i) The simulated results of the OAM Modes +1 and +2. (l)-(o) The measured results of the OAM Modes +1 and +2.

Supplementary Note S8. The EEG signal processing and the detected signal exhibition

Since the EEG signals usually have very low signal-to-noise ratios (SNRs), they are firstly preprocessed, including filtering, down sampling, normalization, and averaging. We concatenate each channel of the preprocessed EEG signal segment to construct a feature vector, denoted as $\mathbf{x} = (x_1, x_2, \ldots, x_D)^\top$, where the length D equals to the product of the number of EEG channels C and the number of time points T for each channel. We consider a model that maps the feature vector $\mathbf{x}$ into label $t \in \{-1, 1\}$, where the label "1" represents the presence of the P300 potential while "−1" represents the absence of the P300 potential. In this

note, we simply derive the Bayesian regression algorithm used for EEG decoding in this study, and readers can refer to Reference [S4] for a more detailed introduction.

The linear combination of $\mathbf{x}$ should be simply with the form of $f(\mathbf{x}, \mathbf{w}) = \mathbf{w}^\top \mathbf{x}$, where $\mathbf{w}$ is the weight parameter. However, for the flexibility of the model, sometimes we will consider a linear combination of fixed basis functions $\phi_j(\mathbf{x})$ of the input variable, with the form

$$y(\mathbf{x}, \mathbf{w}) = \mathbf{w}^\top \boldsymbol{\phi}(\mathbf{x}) \tag{1}$$

where $\mathbf{w} = (w_0, \ldots, w_{M-1})^\top$ and $\boldsymbol{\phi} = (\phi_0, \ldots, \phi_{M-1})^\top$. In this study, we use the basis function $\boldsymbol{\phi}(\mathbf{x}) = \mathbf{x}$, that is, no nonlinear mapping is performed on the preprocessed signal. However, we still use the more general notation $\boldsymbol{\phi}(\mathbf{x})$ instead of $\mathbf{x}$ to make the derivation process and results more universal. We assume that the label t is given by the function $y(\mathbf{x}, \mathbf{w})$ with additive Gaussian noise ε so that

$$t = y(\mathbf{x}, \mathbf{w}) + \varepsilon \tag{2}$$

where $\varepsilon \sim \mathcal{N}(0, \beta^{-1})$, and β is the precision (inverse variance). In this case, we have

$$p(t \mid \mathbf{x}, \mathbf{w}, \beta) = \mathcal{N}(t \mid y(\mathbf{x}, \mathbf{w}), \beta^{-1}). \tag{3}$$

If we consider a dataset with N data points, denoted $\mathbf{X} = (\mathbf{x}_1^\top, \mathbf{x}_2^\top, \ldots, \mathbf{x}_N^\top)^\top \in \mathbb{R}^{N \times D}$ with corresponding labels $\mathbf{t} = (t_1, t_2, \ldots, t_N)^\top \in \mathbb{R}^N$, and assume that these data points are drawn independently from the distribution (3), the likelihood function can be written as follows

$$p(\mathbf{t} \mid \mathbf{X}, \mathbf{w}, \beta) = \prod_{n=1}^{N} \mathcal{N}(t_n \mid \mathbf{w}^\top \boldsymbol{\phi}(\mathbf{x}_n), \beta^{-1}) = \mathcal{N}(\mathbf{t} \mid \boldsymbol{\Phi}\mathbf{w}, \beta^{-1}\mathbf{I}) \tag{4}$$

where $\boldsymbol{\Phi}$ is the design matrix

$$\boldsymbol{\Phi} = \begin{pmatrix} \phi_0(\mathbf{x}_1) & \phi_1(\mathbf{x}_1) & \cdots & \phi_{M-1}(\mathbf{x}_1) \\ \phi_0(\mathbf{x}_2) & \phi_1(\mathbf{x}_2) & \cdots & \phi_{M-1}(\mathbf{x}_2) \\ \vdots & \vdots & \ddots & \vdots \\ \phi_0(\mathbf{x}_N) & \phi_1(\mathbf{x}_N) & \cdots & \phi_{M-1}(\mathbf{x}_N) \end{pmatrix}. \tag{5}$$

The log likelihood function of (4) is as follows

$$\ln p\left(\mathbf{t}\mid\mathbf{X},\mathbf{w},\beta\right)=\sum_{n=1}^{N}\ln\mathcal{N}\left(t_{n}\mid\mathbf{w}^{\top}\boldsymbol{\phi}\left(\mathbf{x}_{n}\right),\beta^{-1}\right)$$

$$=-\frac{\beta}{2}\sum_{n=1}^{N}\left(t_{n}-\mathbf{w}^{\top}\boldsymbol{\phi}\left(\mathbf{x}_{n}\right)\right)^{2}+\frac{N}{2}\ln\beta-\frac{N}{2}\ln\left(2\pi\right). \tag{6}$$

Now we introduce a prior probability distribution over the model parameter $\mathbf{w}$, with the form

$$p\left(\mathbf{w}\mid\alpha\right)=\mathcal{N}\left(\mathbf{w}\mid\mathbf{0},\alpha^{-1}\mathbf{I}\right) \tag{7}$$

where α is the precision parameter of the Gaussian distribution. Since $\mathbf{w}$ and $\mathbf{X}$ are independent, we have

$$p\left(\mathbf{w},\mathbf{t}\mid\mathbf{X}\right)=p\left(\mathbf{t}\mid\mathbf{X},\mathbf{w}\right)p\left(\mathbf{w}\mid\mathbf{X}\right)=p\left(\mathbf{t}\mid\mathbf{X},\mathbf{w}\right)p\left(\mathbf{w}\right), \tag{8}$$

and

$$p\left(\mathbf{t}\mid\mathbf{X}\right)=\int p\left(\mathbf{w},\mathbf{t}\mid\mathbf{X}\right)d\mathbf{w}$$

$$=\int p\left(\mathbf{t}\mid\mathbf{X},\mathbf{w}\right)p\left(\mathbf{w}\mid\mathbf{X}\right)d\mathbf{w} \tag{9}$$

$$=\int p\left(\mathbf{t}\mid\mathbf{X},\mathbf{w}\right)p\left(\mathbf{w}\right)d\mathbf{w}.$$

Therefore, the posterior distribution of $\mathbf{w}$ can be written as follows

$$p\left(\mathbf{w}\mid\mathbf{X},\mathbf{t}\right)=\frac{p\left(\mathbf{w},\mathbf{t}\mid\mathbf{X}\right)}{p\left(\mathbf{t}\mid\mathbf{X}\right)}=\frac{p\left(\mathbf{t}\mid\mathbf{X},\mathbf{w}\right)p\left(\mathbf{w}\right)}{\int p\left(\mathbf{t}\mid\mathbf{X},\mathbf{w}\right)p\left(\mathbf{w}\right)d\mathbf{w}}. \tag{10}$$

Thus,

$$p\left(\mathbf{w}\mid\mathbf{X},\mathbf{t}\right)\propto p\left(\mathbf{t}\mid\mathbf{X},\mathbf{w}\right)p\left(\mathbf{w}\right)=\mathcal{N}\left(\mathbf{t}\mid\boldsymbol{\Phi}\mathbf{w},\beta^{-1}\mathbf{I}\right)\mathcal{N}\left(\mathbf{w}\mid\mathbf{0},\alpha^{-1}\mathbf{I}\right). \tag{11}$$

Through a series of derivations, we have

$$p\left(\mathbf{w}\mid\mathbf{X},\mathbf{t}\right)=\mathcal{N}\left(\mathbf{w}\mid\mathbf{m}_{N},\mathbf{S}_{N}\right) \tag{12}$$

where the mean and variance of the distribution are given by

$$\mathbf{m}_{N}=\beta\mathbf{S}_{N}\boldsymbol{\Phi}^{\top}\mathbf{t}, \tag{13}$$

$$\mathbf{S}_{N}^{-1}=\alpha\mathbf{I}+\beta\boldsymbol{\Phi}^{\top}\boldsymbol{\Phi}. \tag{14}$$

According to Eq. (11), the log of the posterior distribution is given by the sum of the log likelihood and the log of the prior, with the form

$$\ln p\left(\mathbf{w}\mid\mathbf{X},\mathbf{t}\right)=\ln p\left(\mathbf{t}\mid\mathbf{X},\mathbf{w}\right)+\ln p\left(\mathbf{w}\right)+C_{1}$$

$$=-\frac{\beta}{2}\sum_{n=1}^{N}\left(t_{n}-\mathbf{w}^{\top}\boldsymbol{\phi}\left(\mathbf{x}_{n}\right)\right)^{2}-\frac{\alpha}{2}\mathbf{w}^{\top}\mathbf{w}+C_{2} \tag{15}$$

where C_1 and C_2 are both constants. Maximization of this posterior distribution with respect to $\mathbf{w}$ is therefore equivalent to the minimization of the sum-of-squares error function with the addition of a quadratic regularization term

$$\mathcal{L}(\mathbf{w}) = \frac{1}{2}\sum_{n=1}^{N}\left(t_n - \mathbf{w}^\top\boldsymbol{\phi}(\mathbf{x}_n)\right)^2 + \frac{\lambda}{2}\mathbf{w}^\top\mathbf{w} = \frac{1}{2}\|\mathbf{t} - \boldsymbol{\Phi}\mathbf{w}\|^2 + \frac{\lambda}{2}\mathbf{w}^\top\mathbf{w} \tag{16}$$

where $\lambda = \dfrac{\alpha}{\beta}$. Setting the gradient of $\mathcal{L}(\mathbf{w})$ in Eq. (16) to zero, and solving for $\mathbf{w}$, we have

$$\mathbf{w} = \left(\lambda\mathbf{I} + \boldsymbol{\Phi}^\top\boldsymbol{\Phi}\right)^{-1}\boldsymbol{\Phi}^\top\mathbf{t}. \tag{17}$$

Now we introduce prior distributions over the hyperparameters α and β. The marginal likelihood function $p(\mathbf{t}\mid\alpha,\beta)$ is obtained by integrating over $\mathbf{w}$, so that

$$\begin{aligned}
p(\mathbf{t}\mid\alpha,\beta) &= \int p(\mathbf{t}\mid\mathbf{w},\beta)\,p(\mathbf{w}\mid\alpha)\,d\mathbf{w} \\
&= \int\prod_{n=1}^{N}\mathcal{N}\left(t_n\mid\mathbf{w}^\top\boldsymbol{\phi}(\mathbf{x}_n),\beta^{-1}\right)\mathcal{N}\left(\mathbf{w}\mid\mathbf{0},\alpha^{-1}\mathbf{I}\right)d\mathbf{w} \\
&= \left(\frac{\beta}{2\pi}\right)^{\frac{N}{2}}\left(\frac{\alpha}{2\pi}\right)^{\frac{M}{2}}\int\exp\{-\beta\mathcal{L}(\mathbf{w})\}d\mathbf{w}.
\end{aligned} \tag{18}$$

Therefore, the key to calculating $p(\mathbf{t}\mid\alpha,\beta)$ is to calculate $\int\exp\{-\beta\mathcal{L}(\mathbf{w})\}d\mathbf{w}$. Note that we can complete the square over $\mathbf{w}$, so that

$$\beta\mathcal{L}(\mathbf{w}) = \frac{\beta}{2}\|\mathbf{t} - \boldsymbol{\Phi}\mathbf{w}\|^2 + \frac{\alpha}{2}\mathbf{w}^\top\mathbf{w} = \frac{1}{2}(\mathbf{w} - \mathbf{m}_N)^\top\mathbf{S}_N^{-1}(\mathbf{w} - \mathbf{m}_N) + \beta\mathcal{L}(\mathbf{m}_N) \tag{19}$$

where $\mathbf{m}_N$ and $\mathbf{S}_N^{-1}$ are given by Equations (13) and (14), respectively. Substituting Eq. (19) into Eq. (18) gives

$$\begin{aligned}
p(\mathbf{t}\mid\alpha,\beta) &= \left(\frac{\beta}{2\pi}\right)^{\frac{N}{2}}\left(\frac{\alpha}{2\pi}\right)^{\frac{M}{2}}\exp\{-\beta\mathcal{L}(\mathbf{m}_N)\}\int\exp\left\{-\frac{1}{2}(\mathbf{w} - \mathbf{m}_N)^\top\mathbf{S}_N^{-1}(\mathbf{w} - \mathbf{m}_N)\right\}d\mathbf{w} \\
&= \left(\frac{\beta}{2\pi}\right)^{\frac{N}{2}}\left(\frac{\alpha}{2\pi}\right)^{\frac{M}{2}}\exp\{-\beta\mathcal{L}(\mathbf{m}_N)\}(2\pi)^{\frac{M}{2}}\left|\mathbf{S}_N^{-1}\right|^{-\frac{1}{2}}.
\end{aligned} \tag{20}$$

Hence, the log of the marginal likelihood is as follows

$$\ln p(\mathbf{t}\mid\alpha,\beta) = \frac{M}{2}\ln\alpha + \frac{N}{2}\ln\beta - \beta\mathcal{L}(\mathbf{m}_N) - \frac{1}{2}\ln\left|\mathbf{S}_N^{-1}\right| - \frac{N}{2}\ln(2\pi). \tag{21}$$

Now we consider the maximization of $\ln p(\mathbf{t}\,|\,\alpha,\beta)$ with respect to α and β. The partial derivatives of the log of the marginal likelihood with respect to α and β are respectively given by

$$\frac{\partial}{\partial\alpha}\ln p(\mathbf{t}\,|\,\alpha,\beta) = \frac{M}{2\alpha} - \frac{1}{2}\mathbf{m}_N^\top\mathbf{m}_N - \frac{1}{2}\sum_i\frac{1}{\lambda_i+\alpha}, \tag{22}$$

$$\frac{\partial}{\partial\beta}\ln p(\mathbf{t}\,|\,\alpha,\beta) = \frac{N}{2\beta} - \frac{1}{2}\sum_{n=1}^{N}\left(t_n - \mathbf{m}_N^\top\boldsymbol{\phi}(\mathbf{x}_n)\right)^2 - \frac{\gamma}{2\beta}, \tag{23}$$

where λ_i are the eigenvalues of $\beta\boldsymbol{\Phi}^\top\boldsymbol{\Phi}$, and $\gamma = \sum_i\frac{\lambda_i}{\alpha+\lambda_i}$. Setting $\frac{\partial}{\partial\alpha}\ln p(\mathbf{t}\,|\,\alpha,\beta) = 0$

and $\frac{\partial}{\partial\beta}\ln p(\mathbf{t}\,|\,\alpha,\beta) = 0$, we see that the solution of α and β that maximize the marginal likelihood (20) satisfies

$$\alpha = \frac{\gamma}{\mathbf{m}_N^\top\mathbf{m}_N}, \tag{24}$$

$$\beta = \frac{N-\gamma}{\displaystyle\sum_{n=1}^{N}\left(t_n - \mathbf{m}_N^\top\boldsymbol{\phi}(\mathbf{x}_n)\right)^2}. \tag{25}$$

Since the variable $\mathbf{m}_N$ and γ depend on α and β, the solution is self-contained. Therefore, these parameters should be updated iteratively. We summarize the training procedure as follows.

Algorithm 1 Training Procedure for Bayesian Linear Regression

---

Input: Training samples $\left\{\boldsymbol{\phi}(\mathbf{x}_i),t_i\right\}_{i=1}^{N}$, where $\mathbf{x}_i\in\mathbb{R}^D$, $\boldsymbol{\phi}(\mathbf{x}_i)\in\mathbb{R}^M$, and $t_i\in\mathbb{R}$.

Output: Weight parameter $\mathbf{w}$.

Construct the design matrix $\boldsymbol{\Phi} = \left(\boldsymbol{\phi}(\mathbf{x}_1)^\top,\ \boldsymbol{\phi}(\mathbf{x}_2)^\top,\ldots,\ \boldsymbol{\phi}(\mathbf{x}_N)^\top\right)^\top$.

Set the values of $d_\mathbf{w}$, $n_{\max}$, and ϵ_{stop}.

Choose an initial setting for $\alpha^{(0)}$ and $\beta^{(0)}$.

Calculate $\mathbf{S}_N^{(0)}$ using Eq. (14).

Calculate $\mathbf{m}_N^{(0)}$ using Eq. (13).

Calculate all eigenvalues λ_i of $\mathbf{\Phi}^\top\mathbf{\Phi}$.

$n_{\text{iter}} \leftarrow 1$.

while $d_{\mathbf{w}} > \epsilon_{\text{stop}} \vee n_{\text{iter}} \leq n_{\max}$ **do**

    Calculate $\mathbf{S}_N^{(n_{\text{iter}})}$ using Eq. (14).

    Calculate $\mathbf{m}_N^{(n_{\text{iter}})}$ using Eq. (13).

    Calculate $\gamma^{(n_{\text{iter}})} = \sum_i \dfrac{\beta^{(n_{\text{iter}}-1)}\lambda_i}{\alpha^{(n_{\text{iter}}-1)} + \beta^{(n_{\text{iter}}-1)}\lambda_i}$.

    Calculate $\alpha^{(n_{\text{iter}})}$ using Eq. (24).

    Calculate $\beta^{(n_{\text{iter}})}$ using Eq. (25).

    Calculate $d_{\mathbf{w}} = \dfrac{\|\mathbf{m}^{(n_{\text{iter}})} - \mathbf{m}^{(n_{\text{iter}}-1)}\|}{\|\mathbf{m}^{(n_{\text{iter}}-1)}\| + \epsilon}$, where ϵ is a small value (e.g., 10^{-32}).

    $n_{\text{iter}} \leftarrow n_{\text{iter}} + 1$.

end while

$\mathbf{w} = \mathbf{m}_N^{(n_{\text{iter}}-1)}$.

In online manipulation stage, for a specific signal segment, the confidence score is calculated simply using Eq. (1).

To further exhibit the EEG signals collected in the experiments, we present eight segments in the visual beam-scanning scheme, as listed in Fig. S13. The target and nontarget curves represent the signals with and without stimulus, marked in orange and blue. The averaging operation is meant to improve the signal-to-noise ratio (SNR) and enhance the characteristics of the waveforms. Although EEG signals are usually very noisy and with an extremely low SNR, a positive potential, namely P300, can still be seen from the averaged EEG waveforms at about 300 ms after the stimuli of the target. Since the operator does not receive the flashing stimuli from the nontarget buttons, the P300 potential does not appear when the nontarget
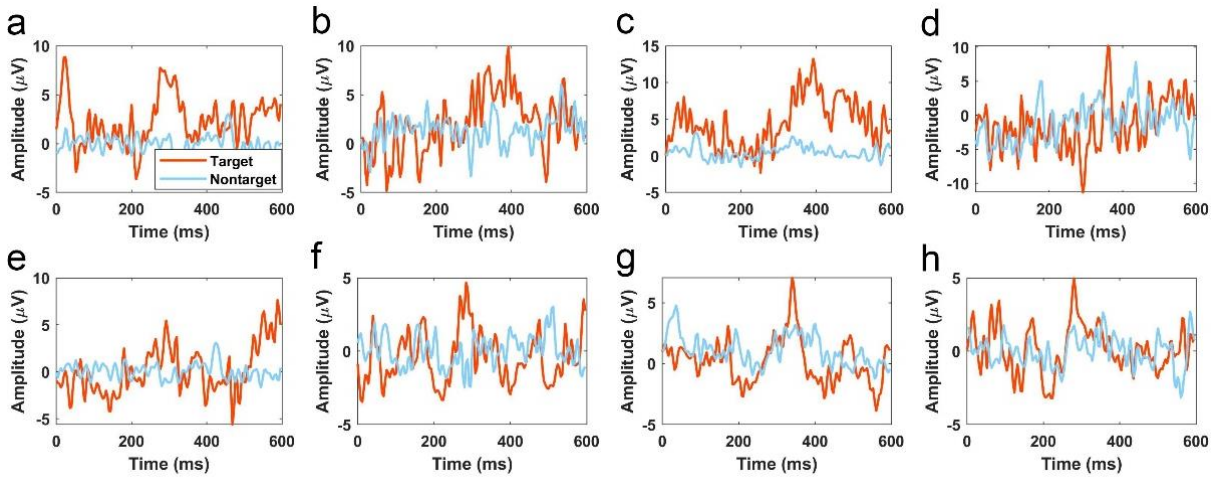
buttons flash.

Fig. S13. The measured EEG signal comparison between the target and nontarget. (a)-(h) The measured signals in the visual beam-scanning scheme.

Supplementary Note S9. The detailed illustration and the related simulation results in pattern encoding scheme

We establish a demonstration prototype as shown in Fig. 5a. The operator equipped with BCI device stares at the GUI screen to actuate the metasurface. In the metasurface pattern coding scheme, we verify that EBCM can achieve 2-bit phase coding patterns directly from the brain signals, therefore allowing arbitrary scattering signatures. The encoding GUI is illustrated in Fig. S14a, where we present a 4×10 button matrix for 2-bit 10×10 code input. The encoding GUI is a matrix with 4 rows and 10 columns, labeled as 'A0' to 'D9'. Here, we apply the first two rows for row coding, where the two digits in the same column are used as the first and second digits of a 2-bit binary number. For example, if 'A0' and 'B0' are encoded as '1' and '0' respectively, the binary number '10' corresponds to the quaternary number '2'. Similarly, the column coding process is determined by the third and fourth rows. The row and column coding sequences ('0210121321' and '0323101332') respectively determine the code distribution along the x-axis and y-axis, superposing the final coding pattern in Fig. S14b. Four green colors with different brightness indicate the four phase states encoded within the quaternary numbers. It should be noted that each code represents a 2×2 supercell, which means that the metasurface is composed of 20×20 elements. Before the encoding process, each code is set to '0' by default and can be set to '1' by operator's staring. When the encoding process is completed, the

generated coding pattern is immediately sent to FPGA to activate the corresponding diode voltage distribution. The related video of the pattern encoding process is recorded and provided in Supplementary Movie S4.
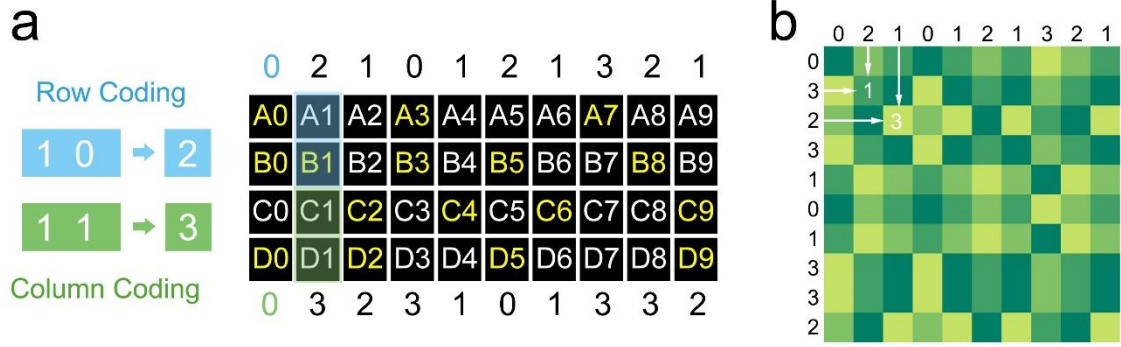

Fig. S14. The illustration of the interface for pattern encoding and an encoded pattern example. (a) GUI of the metasurface pattern encoding, where the first two rows for metasurface row-coding and the last two rows for metasurface column-coding. The buttons set to '1' in the experiment are marked by yellow characters. (b) The encoded pattern from the BCI operator, in which each block indicates a 2×2 supercell. The calculation method of the coding pattern conforms to the quaternary addition.

In the pattern encoding scheme, the input code represents a 2×2 supercell (4 units with the same phase state). As shown in Fig. S14, the complete coding sequences of row and column are "33110033001100221100" and "11003300221122000033" respectively. The superposition principle of the two sequences is the same as the original coding metasurface theories [S1-S3], and the complete pattern is shown in Fig. S15a. According to the interface given in Fig. S15b, the encoding process starts from the first row by gazing the button and stops encoding by staring at any previously sent button. For example, if the button "D7" is the final code, inputting any codes before "D7" (A0-D6) after inputting "D7" is regarded as the stop instruction. The final encoded interface is given in Fig. S15c, where yellow block represents "1" and blue block represents "0". The initial state of the interface is all blue and the buttons can be transformed into yellow (set as "1"). The calculation of 2-bit coding sequence is calculated according to the following equations:

$$\text{Column\_sequence(i)} = 2 * c_1(i) + c_2(i), \quad \text{Row\_sequence(i)} = 2 * r_1(i) + r_2(i). \tag{26}$$

where c_1, c_2 are the first and second bits of column, and r_1, r_2 are the first and second bits of row as shown in Fig. S15c. To match the control panel of P300 BCI devices, we apply the

interface with 4×10 buttons for demonstration and exhibition. It should be noted that the encoding interface can be further enlarged for more coding information input by using a larger scale interface. The simulated field presents a single beam deflection as provided in Figs. S15d and S15e, which reveal a good RCS reduction performance. Both 2D and 3D versions of the simulation data is listed in Figs. S15d and S15e. The full-wave simulation is performed in the CST Microwave Studio with open boundary condition. Another two examples of encoding function are showed in Figs. S15f and S15g, respectively realizing dual-beam and four-beam fields. The coding pattern of dual-beam is derived from the sequence "00022200022200022200", whose code varies only along x-axis, as shown in Fig. S15f. We provide the related result of simulation in Fig. S15f, revealing two symmetrical beams at about ±27°. Fig. S15g exhibits the chessboard pattern to produce four-beam field.

References

[S1] T. J. Cui, M. Q. Qi, X. Wan et al., "Coding metamaterials, digital metamaterials and programmable metamaterials," Light: Science & Applications, vol. 3, no. 10, pp. e218-e218, Oct, 2014.

[S2] S. Liu, T. J. Cui, L. Zhang et al., "Convolution Operations on Coding Metasurface to Reach Flexible and Continuous Controls of Terahertz," Advanced Science, vol. 3, no. 10, pp. 1600156, Oct, 2016.

[S3] Q. Ma, G. D. Bai, H. B. Jing et al., "Smart metasurface with self-adaptively reprogrammable functions," Light-Science & Applications, vol. 8, no. 1, pp. 98, 2019.

[S4] Bishop, C. M. Pattern Recognition and Machine Learning. 1 edn, pp. 137-173 (Springer-Verlag New York, 2006).
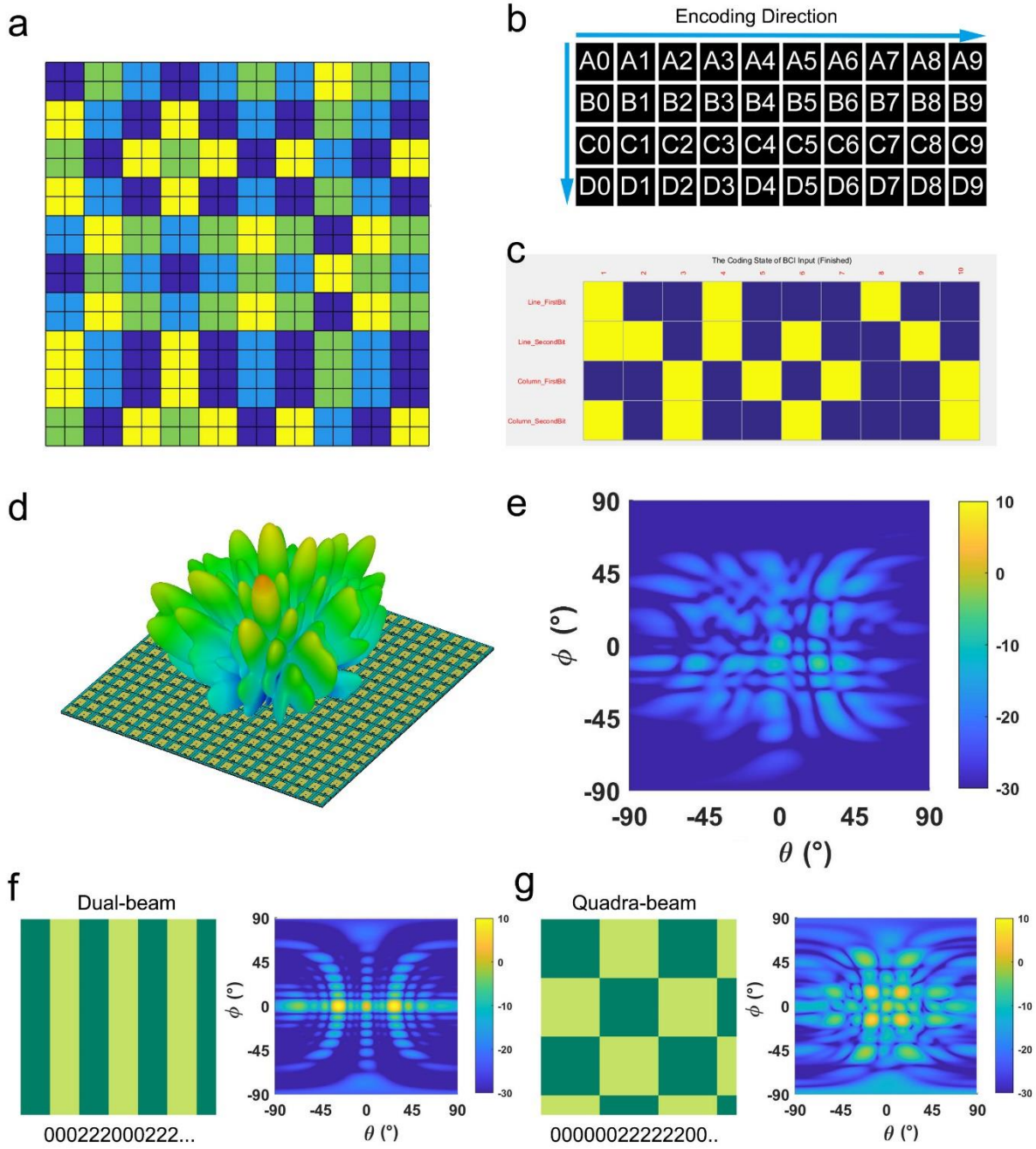
Fig. S15. The illustration of the encoding pattern and interface as well as its simulation result. (a) The final coding pattern of the encoding scheme. (b) The encoding interface for BCI operator. (c) The real-time interface of the encoded data. (d) and (e) The 3D and 2D simulated far-field result for the coding pattern in (a). (f) and (g) The encoding examples of dual-beam and quadra-beam patterns and their simulation results.

Supplementary Movies

Movie S1.

The wireless text-communication process is presented in this movie. The transmission of five letters 'HELLO' are exhibited. The last received letter is shown on the receiver's screen.

Movie S2.

The visual beam-scanning experiment is presented in this movie. The operator directly achieves the desired beam-scanning direction by visually staring at the specific direction. The executed coding pattern for the related beam-scanning direction is exhibited on the LED-version metasurface after the EBCM detects the operator's EEG. Four typical patterns are shown in this movie.

Movie S3.

The versatile wavefront synthesis of five typical EM functions within the EBCM is presented in this movie, including one RCS reduction, two beam-deflections and two OAM beams. The related coding pattern is displayed on the metasurface after the EEG detection.

Movie S4.

The pattern encoding process with EBCM is presented in this movie. The operator inputs the desired code by staring the specific button. The inputted codes that detected by EBCM are displayed on the screen with yellow blocks. The last code 'C4' is a stop instruction to end the encoding process and command FPGA calculate the final coding pattern. After that, the EBCM executes the calculated coding pattern, as exhibited on the LED-version metasurface.